Binary γ-Al$_2$O$_3$–α-Ga$_2$O$_3$ as supports of NiW catalysts for hydrocarbon sulfur removal

CrossMark

J.N. Díaz de León

Universidad Nacional Autónoma de México, Centro de Nanociencias y Nanotecnología, Carretera Tijuana-Ensenada Km. 107, 22800 Ensenada, BC, Mexico

ARTICLE INFO

ABSTRACT

A series of γ-Al$_2$O$_3$–α-Ga$_2$O$_3$ binary mixed supports with different Ga$_2$O$_3$ content (labeled AlGa-*x*, where *x* is the wt.% of Ga$_2$O$_3$) were synthesized by a one-step precipitation method and calcination. These supports were used to prepare NiW catalysts and later tested in the hydrodesulfurization (HDS) reactions of gasoline and diesel model sulfur compounds. Morphology, surface and electronic properties of AlGa-*x* samples changed considerably depending on Ga$_2$O$_3$ content. Amorphous alumina and low gallium oxide content samples showed higher WS$_2$ dispersion when compared with the gallium-free sample by HRTEM analysis. All materials displayed excellent catalytic activity in the 3-methyl-thiophene (3MT) and dibenzothiophene HDS reactions. The best catalytic performance for both tests was obtained with the NiW/AlGa-25 sulfided catalyst. Furthermore, hydrogenation capacity was clearly modified by the presence of GaAl$_2$O$_4$ spinels as well as α-Ga$_2$O$_3$. In the 3MT HDS reaction, the presence of isoprene among the reaction products showed that, using the NiW/AlGa-*x* catalyst, this reaction may be successfully conducted by the desulfurization pathway. Noteworthy was the formation of well-defined microcrystals in samples with the highest gallium oxide content. Results from this work reveal that the binary γ-Al$_2$O$_3$–α-Ga$_2$O$_3$ mixed oxides have great potential as support for hydrocarbon sulfur removal catalysts.

© 2015 Elsevier B.V. All rights reserved.

1. Introduction

During the last decade, a great concern to produce clean diesel and gasoline fuels has been expressed by the refining industry. To meet the sulfur specifications for highway transportation vehicle fuels, deep sulfur removal from refractory molecules has to be done [1]. The complex fractions obtained from Mayan crude oil represent quite a challenge for Mexican refinery units because the concentration of sulfur in light cycle oil (LCO) may reach up to 31,000 parts per million (ppm S) [2] and nitrogen-containing compounds from 800 to 1000 ppm [3]. To attain deep hydrodesulfurization (HDS), sulfur must be removed from dibenzothiophene (DBT) and 4,6′dimethyl-DBT (4,6′DM-DBT). However, these compounds have the lowest reaction rates among the bulk of sulfur compounds [4,5]. Typically, HDS reactions are catalyzed by CoMo/γ-Al$_2$O$_3$ or NiMo/γ-Al$_2$O$_3$ while NiW/γ-Al$_2$O$_3$ is scarcely used. This is probably because WO$_x$ species are more difficult to transform into sulfide species than MoO$_x$ [6] due to their strong interaction with the alumina carrier. Thus, the formation of the WS$_2$ phase may be improved by modifying the γ-Al$_2$O$_3$ carrier [7] or using alternative supports [8]. Besides,

the ability of alumina to host certain ions is widely recognized, e.g. of atoms involved in the promotion of the active phases such as Co or Ni. These atoms react with the surface of alumina and form external layers of spinel aluminates [9]. This Co or Ni-alumina interaction may be avoided by doping the alumina carrier. Recent studies have shown enhancement of the catalytic properties of sulfided materials by the inclusion of additives [10–13]. The ions used as additives normally fill out the tetrahedral sites in the alumina surface structure, avoiding migration phenomena [12]. Likewise, the nature of the support changes the interaction with the active phase, e.g. titania and zirconia induced higher catalytic activity compared with alumina supported catalysts (Mo or W) [14]. Recently, gallium has attracted widespread attention in HDS catalysts, e.g. as mixed oxide with alumina [15,16], as promoter [17], as additive [10–12] and as dual catalyst [6]. Further, gallium oxide and Al$_2$O$_3$–Ga$_2$O$_3$ mixed oxides are effective catalysts with various applications such as selective catalytic reduction of NOx, and paraffin dehydrogenation to olefin, among others [18]. The aim of this work was to determine the effect of binary Al$_2$O$_3$–Ga$_2$O$_3$ mixed oxides as an alternative support for NiW HDS catalysts. Pure Al$_2$O$_3$, Ga$_2$O$_3$ as well as mixed Al$_2$O$_3$–Ga$_2$O$_3$ materials were prepared by a modified coprecipitation method. Samples were characterized by a wide variety of techniques such as N$_2$ adsorption/desorption isotherms, X-ray diffraction (XRD), UV–vis diffuse reflectance spectroscopy (DRS),

X-ray photoelectron spectroscopy (XPS), electrophoretic measurements, scanning electron microscopy (SEM) and high resolution transmission electron microscopy (HRTEM). Prepared catalysts were tested in hydrodesulfurization reactions of typical refractory model compounds of gasoline (3-methyl-thiophene) and diesel (DBT) fuels.

2. Experimental

2.1. Synthesis of supports

The Al_2O_3–Ga_2O_3 samples (labeled AlGa-*x*, where *x* is the wt.% of Ga_2O_3) were synthesized using a one-step precipitation method, modified from a previous report [19]. For each sample (*x* = 0, 25, 50, 75, and 100%), 2 g of support were obtained from $Al(NO_3)_3 \cdot 9H_2O$ (Aldrich-Chemical, 99.99%) (14.7, 11.0, 7.3, 3.6 and 0 g) and $Ga(NO_3)_3 \cdot 8H_2O$ (Aldrich-Chemical, 99.99%) (0, 2.1, 4.2, 6.4 and 8.5 g). The synthesis solutions were prepared using 80 mL of deionized water to which was added the amount of selected precursor described above. This solution was quickly added to a stirred solution of 150 mL H_2O and 52.5 mL NH_4OH (58%) as precipitant agent and stirred for 1 h. The white solids were dried at 358 K and then calcined at 773 K for 4 h (1 K min^{-1}).

2.2. Catalyst preparation

NiW catalysts were prepared by successive impregnation of the support, using the pore-filling method, with aqueous solution of ammonium metatungstate (AMT) (($NH_4)_6W_{12}O_{39} \cdot xH_2O$, Aldrich-Chemical, 99.99%) and nickel nitrate ($Ni(NO_3)_2 \cdot 6H_2O$, Aldrich-Chemical, 99.99%). Ammonium metatungstate (AMT) impregnation was performed at pH 3.7 and nickel impregnation with a nickel nitrate solution at pH 4.4. The AMT solution concentration was selected in order to obtain 16 wt.% of W (pH 3.7) while that of nickel was adjusted to define a nominal atomic ratio $r = Ni/(Ni + W)$ equal to 0.31. In a typical preparation, the AMT solution was firstly impregnated on the support, left to macerate for 12 h, and then the solid was dried under a stream of air at 398 K for 12 h, with a heating rate of 3 K min^{-1}. Afterward, Ni was impregnated under the same conditions, and the final solid was calcined at 723 K for 4 h with a heating rate of 1 K min^{-1}. A commercial NiW/γ-Al_2O_3 catalyst was used as reference (~20 wt.% of W and ~4 wt.% of Ni), its catalytic activity on HDS of DBT was reported in a previous work [7].

2.3. Characterization techniques

Nitrogen adsorption–desorption isotherms were obtained at 77 K over the whole range of relative pressures, using a Tristar-II 3020 BET equipment on samples previously degassed at 373 K for 4 h. BET-specific areas (S_{BET}) were calculated from these isotherms using the BET method with a value of 0.162 nm^2 for the cross-section of the physically adsorbed N_2 molecule. Average pore size (P_s) was determined by using the Barett–Joyner–Halenda (BJH) model to the desorption branch of the isotherms. X-ray diffraction (XRD) measurements were taken using a spectrometer (Philips, model X'pert) with Cu Kα radiation (40 kV, 30 mA) at a wavelength of 0.154 nm. UV–vis diffuse reflectance spectra were recorded in the 200–700 nm range at room temperature with a UV–Vis spectrophotometer (Varian Cary-300) equipped with an integration sphere. Reflectance data were converted to Kubelka–Munk function F (%R) values. The absorption edge energies were obtained as described by Barton et al. [20]. X-Ray photoelectron spectroscopy (XPS) was recorded using a Riber LDM-32. Energy positions of the peak maxima were calibrated using the BE of the C 1s peak from the tape at 284.6 eV as a reference to correct the spectra. Electrophoretic

measurements were obtained using a Zetasizer Nano ZS instrument, based on electrophoretic light scattering. A total of 300 mg of the particles were ultrasonically dispersed in 300 mL of 10^{-3} M KCl solution. The pH value was adjusted with 1^{-3} M HCl or KCl solution. Low and high-resolution images were obtained by scanning electron microscopy (SEM) (JEOL-JSM-5300) and (JEOL JIB-4500), respectively. High-resolution transmission electron microscopy (HRTEM) micrographs were collected with a JEOL-2010F instrument. The samples were suspended in heptane as a solvent to be deposited on a lacey carbon (440 mesh) Cu grid. Average slab length (*L*) and the stacking number (*N*) were calculated from an examination of more than 550 particles. Statistical analyzes were done as described elsewhere [12].

2.3.1. Catalytic evaluation

2.3.1.1. HDS of DBT (batch reactor). Catalytic activity was tested with a diesel model sulfur compound in a batch Parr reactor at 593 K and hydrogen pressure of 5.5 MPa. Prior to each reaction, the catalysts were activated by ex-situ sulfidation using a mixture of H_2/H_2S 15 vol.% H_2S with a flow of 40 mL min^{-1} at and 673 K for 2 h (5 K min^{-1}). The reactor was loaded with approximately 0.2 g of sulfided catalyst (−80/+100 mesh), 500 ppm of S from DBT and 100 mL of *n*-hexadecane as a solvent. Reaction products were analyzed by GC on an Agilent 7890 instrument, using an Agilent 30 m HP-5 capillary column. Catalytic activity was expressed by the initial reaction rate (mol DBT transformed per second and per gram of catalyst).

2.3.1.2. HDS of 3-methyl-thiophene (continuous flow reactor). The 3MT HDS reactions were performed at atmospheric pressure in a biphasic continuous micro-flow reactor. The saturator with chromatographic 3MT (Aldrich-Chemical 99.9%) was maintained at 293 K, and then 40–100 cm^3 min^{-1} of H_2 flow were sent through it. The flow was controlled at an adequate value to avoid high conversions (~70 cm^3 min^{-1}). The catalytic reaction was tested at 553 K at steady state using around 50–100 mg of pre-activated catalyst. All catalysts were previously stabilized at 640 K for 5 h. The products were analyzed by GC, and all rates were estimated at low conversion (<15%) once the steady state conditions were reached. All reaction products were analyzed by online-GC on an Agilent 7890 instrument, equipped with an Agilent 30 m HP-5 capillary column. The catalytic activity was expressed by the steady state reaction rate (mol$_{3MT}$ transformed per second and per gram of catalyst).

3. Results

3.1. Textural properties

The nitrogen adsorption–desorption isotherm was type IV for all samples, which is characteristic of mesoporous materials (Fig. 1A). Especially, samples AlGa-25 and AlGa-50 showed typical isotherms obtained from mixed oxides [21]. The hysteresis loops exhibited a wide variety of shapes. In accordance with IUPAC recommendations, samples AlGa-25 and AlGa-50, which displayed an H1 hysteresis loop, are related to a narrow distribution of uniform pores. In the case of AlGa-0, AlGa-75, and AlGa-100, H2 hysteresis was observed; this indicates that the distribution of pore sizes and shapes is not well-defined [22].

The pore size distribution of all samples is depicted in Fig. 1B. Samples AlGa-0 to AlGa-75 showed a peak centered near 33 Å. The distribution of the AlGa-0 sample was asymmetric with a wide shoulder that ended at around 150 Å. For samples AlGa-25 and AlGa-50, the desorption branch indicated almost unimodal pore size distribution. The full textural properties are listed in Table 1. As shown, the AlGa-0 sample showed 246 m^2 g^{-1}, a specific surface area value typically obtained for pure commercial alumina.
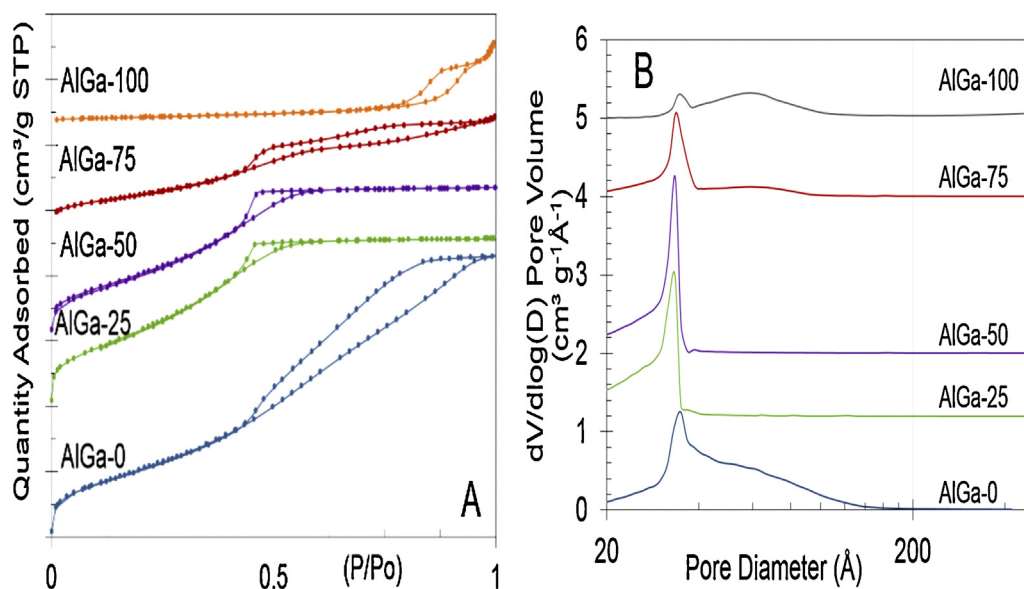
Fig. 1. (A) Nitrogen adsorption isotherms at 77 K of AlGa-x series. (B) Pore size distributions.

Table 1
Textural properties for AlGa-x series. Samples calcined at 773 K.

Samples[a]	S_{BET}	Pv	Ps[b]
	$m^2\,g^{-1}$	$cm^3\,g^{-1}$	Å
AlGa-0	246	0.35	57
AlGa-25	280	0.22	32
AlGa-50	230	0.20	38
AlGa-75	118	0.13	46
AlGa-100	21	0.08	150

[a] Samples calcined at 773 K.
[b] Average pore size.

The addition of 25 wt.% of gallium oxide produced a 14% higher S_{BET} in AlGa-25 than in AlGa-0. AlGa-25 also displayed the largest

specific surface area among all AlGa-x materials. Further addition of gallium oxide caused a decrease in textural properties.

3.2. Crystalline phases

XRD patterns of all samples are shown in Fig. 2. AlGa-0 showed very broad peaks at 37°, 46° and 66.8°, attributed to the planes (1 1 1), (1 0 0) and (1 1 0) of the γ-Al_2O_3 phase. Materials AlGa-25 and AlGa-50 displayed the same low intensity alumina peaks as alumina and a low intensity peak around 36° related with the Ga_2O_3 content and corresponding to the solid solution formation [23]. In the AlGa-75 and AlGa-100 patterns, high intensity peaks appeared at 24.5°, 33.8°, 36.0°, 41.45°, 50.25°, 55.15°, 59.05°, 63.35°, and 64.75° corresponding to a trigonal-rhombohedral crystalline system for the α-Ga_2O_3 phase. The high-intensity peaks of the α-Ga_2O_3 phase exhibited by these two samples (AlGa-75 and
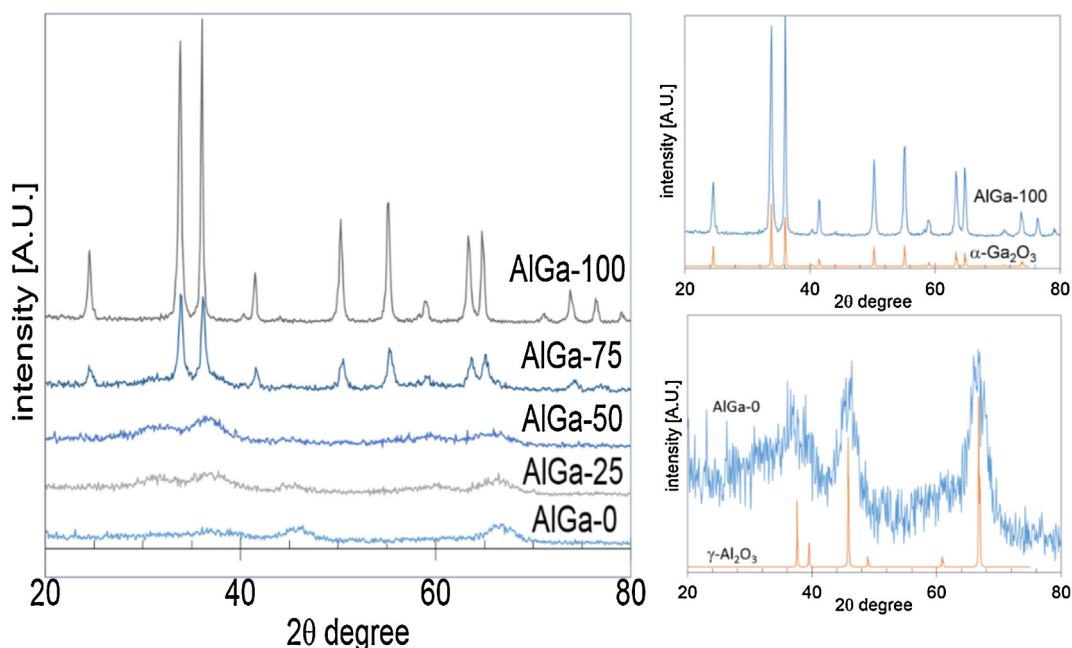

Fig. 2. X-ray diffraction patterns correspondent to AlGa-x series calcined at 773 K.
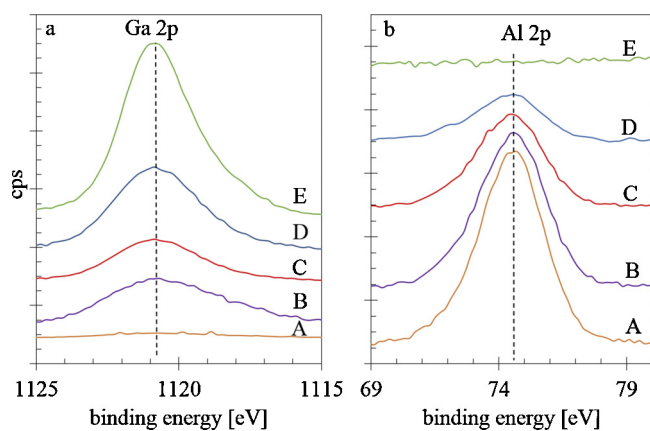
Fig. 3. XPS Ga 2p (a) and Al 2p (b) core levels spectra for the AlGa-*x* series.

Table 2
XPS Ga/(Ga + Al) atomic emission intensity ratio.

Ga/(Ga + Al) atomic ratio					
Ratio	AlGa-0	AlGa-25	AlGa-50	AlGa-75	AlGa-100
XPS	0	0.31	0.45	0.62	1.0
Theoretical	0	0.15	0.35	0.62	1.0

AlGa-100) allowed the indexation of these patterns as a single crystalline phase due to the γ-Al_2O_3 phase short-range crystallinity. Typical shifts towards lower Bragg angles and reflections arising from the cubic $GaAl_2O_4$ spinel-type structures (space group Fd3m) [24] were not observed in any of the XRD patterns. Nevertheless, as the local spinel-type structures could be below the XRD detection limit (crystallites < 4 nm), their potential presence was analyzed by XPS, electrophoretic measurements, and HRTEM techniques.

3.3. X-ray photoelectron spectroscopy (XPS)

Fig. 3 shows the spectra of the Ga 2p (a) and Al 2p (b) core levels for the AlGa-*x* series. As expected, the binding energy corresponding to the Ga 2p emission appeared in the region between 1124 and 1116 eV. In general, with the rise in gallium content an increase in emission intensity was observed, although the emission intensity obtained for AlGa-25 (Fig. 3a-B) and AlGa-50 (Fig. 3a–C) was quite similar. The AlGa-75 sample showed higher intensity than the AlGa-25 and AlGa-50 samples. The XPS emission observed at low binding energies (19.3 eV) for Ga 3d was unsuitable for qualitative or quantitative analyzes, due to its partial overlap with the O 2s peak. In contrast, the corresponding XPS emission region of Al 2p (69–80 eV), showed the opposite behavior. In this case, the intensity seemed to decrease as a function of the aluminum oxide content for all materials. In order to obtain further information, the Ga/(Ga + Al) atomic ratios of the samples were calculated and are summarized in Table 2. The atomic ratio variation revealed that the samples AlGa-25 and AlGa-50 had gallium-enriched surface compositions. For the AlGa-75 sample, the experimental ratio was exactly the same as the theoretical ratio, suggesting a homogeneous gallium/aluminum concentration from the surface to bulk. These results can be associated with a gradient concentration inside the particles, probably because the alumina structure allowed the formation of surface stoichiometric $GaAl_2O_4$ spinels [18], which is reflected in the gallium-enriched surface.

3.4. Surface charge (Electrophoretic analysis)

Fig. 4 shows the relationship between the zeta potential and pH for the AlGa-*x* series. Obtained data allowed to determine the
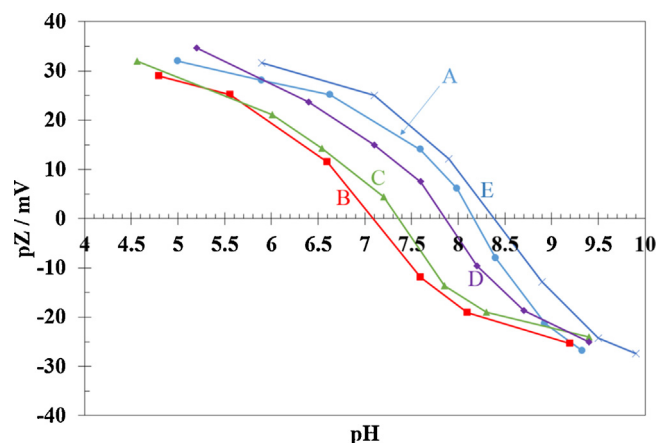

Fig. 4. Zeta potential at 298 K as a function of suspension pH for AlGa-0 (A), AlGa-25 (B), AlGa-50 (C), AlGa-75 (D) and AlGa-100 (E).

zero point of charge (ZPC) for all samples. The pH values were as follows: 8.05, 7.09, 7.36, 7.86, and 8.39 for AlGa-0, AlGa-25, AlGa-50, AlGa-75, and AlGa-100, respectively. The ZPC is a function of the isoelectric point (IEP), and the superficial molar fraction of each phase in the material is described by the following equation: $ZPC = \Sigma IEP \times x_i$ where, x_i corresponds to the superficial molar fraction [11]. Thus, the ZPC of the AlGa-0 and AlGa-100 should be the IEP of the γ-Al_2O_3 and the α-Ga_2O_3, respectively. The ZPC of the most frequently studied specimens of Al_2O_3 are in the range of 8.5–9 and the commercial Ga_2O_3 is reported as 9 [25]. Due to the above equation, a binary mixed material composed of Al_2O_3 with an IEP of around 8 and Ga_2O_3 with IEP of 8.4 on the surface, should increase its ZPC. Nevertheless, a clear decrease was observed for the binary samples, indicating the possible presence of compounds with low IEP, meaning the solid solution and $GaAl_2O_4$ spinels (depending on the mixed Ga-O-Al oxide sites content in the sample). To the best of our knowledge, neither the IEP nor the ZPC of a γ-Al_2O_3–α-Ga_2O_3 solid solution have been reported before. Consequently, the question arises if this solid solution would have an intrinsically lower ZPC than purer oxides. Indeed, previous sections mentioned the possible formation of superficial $GaAl_2O_4$. This result supports the assumption, since the IEP of gallium aluminate was reported to be 4.2 [11].

3.5. UV–vis diffuse reflectance spectroscopy

Diffuse reflectance spectroscopy results are depicted in Fig. 5. As expected, the AlGa-0 sample exhibited a small and wide absorption shoulder in the region of 205–232 nm with maximum intensity around 215 nm (Fig. 3A). This region corresponds to the ligand metal charge transfer transitions from O^{2-} to Al^{3+} [26]. The binary materials AlGa-25 (B) and AlGa-50 (C) showed the same absorption but higher intensity with the increment in gallium oxide content. This effect is related to the appearance of the AlGa solid solution. Nevertheless, the formation of $GaAl_2O_4$ by the inclusion of the Ga^{3+} cations into the alumina structure should be taken into account, as proposed above. The great affinity of Ga^{3+} to the tetrahedral sites of alumina could explain the absorption intensity amplification observed in this region (where normally tetrahedral species with large edge energies appear). It is widely recognized that, in mixed oxides, Ga^{3+} and Al^{3+} ions occur in both tetrahedral and octahedral sites of the spinel-type structures, although tetrahedral sites are preferentially occupied by Ga^{3+} ions [27]. Indeed, according to the bands observed in Fig. 5, the region corresponding to the absorption of tetrahedral species increases with the gallium oxide content. Materials with higher gallium oxide wt.%, i.e., AlGa-75 and
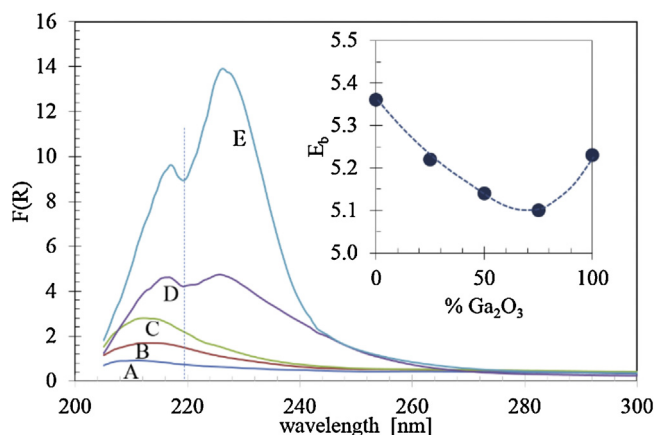
Fig. 5. UV–vis diffuse reflectance absorption spectra of AlGa-x samples (A) AlGa-0, (B) AlGa-25, (C) AlGa-50, (D) AlGa-75 and (E) AlGa-100. Absorption edge energies are determined by the intercept of a linear fit to the absorption edge (inset).

AlGa-100, show an extra shoulder in the region of 220–270 nm with maximum intensity located at about 227 nm. This absorption was associated with the α-Ga_2O_3 and other gallium oxide polymorphs [28]. The absorption edge energies (E_b) for the AlGa-x series were obtained by plotting $[F(R_\infty) \times \hbar\nu]^2$ vs $\hbar\nu$. Some examples are provided as supplementary information (S1). This calculation yields band gap energies of 5.36, 5.22, 5.14, 5.10, and 5.23 eV for materials AlGa-0 to AlGa-100, respectively (as an inset in Fig. 5). Normally, the insulating character of γ-alumina is reflected by an energy gap as high as 7.2 eV [7]. As shown, none of the AlGa-x materials exhibited such a large energy gap. It was particularly unexpected in the case of the AlGa-0 sample due to evidence obtained from XRD, where the pattern confirmed the formation of the γ-Al_2O_3 phase. The binary samples AlGa-25 (5.22 eV), AlGa-50 (5.14 eV), and AlGa-75 (5.10 eV) revealed a decrease in E_b as the gallium oxide content increased. This is consistent with the band gap energies reported for pure gallium polymorphs, which are usually in the range of 4.2–4.9 eV [28,29]. The obtained E_b values followed the trend: AlGa-0 > AlGa-100 > AlGa-25 > AlGa-50 > AlGa-75. It should be noted that the band gap for the AlGa-100 material (5.23 eV), differs from other reported values for the α-Ga_2O_3 phase (4.56 eV) [28]. This difference in band gap energies may be caused by a modification in the lattice structure related to the crystallinity observed by XRD, because structural variations of this kind frequently shift the electronic band in metal oxides [30]. Moreover, it is interesting to compare the E_b for γ-Al_2O_3 (5.36 eV) with that obtained for α-Ga_2O_3 (5.23 eV). As mentioned, a much larger E_b value would be expected for the γ-Al_2O_3 than for the α-Ga_2O_3 due to the absence of tetrahedrally coordinated cations in alumina. Recently, a reduction in the band gap energy for γ-Al_2O_3 materials was reported; the authors directly related this variation of the conduction character to the size and shape of the nanostructured material [7]. Therefore, further characterization by SEM and HRTEM is discussed below.

3.6. Morphological characterization

3.6.1. Scanning electron microscopy (SEM)

Striking morphological differences were observed among the solids at the microscopic level with the variations in gallium oxide content. The AlGa-0 (Fig. 6A) and AlGa-25 samples showed agglomerated irregularly shaped particles in the range of 20–60 μm. These materials seem to be formed by irregular and densely packed layers since no smaller agglomerated structures were detected up to the limit of SEM magnification. In the case of AlGa-50 and AlGa-75, some single micro-crystallites (Fig. 6B) and a high number of rectangular arrays of prism-shaped particles (Fig. 6C) were clearly

observed. The microcrystallites measured an average length of 3.42 μm and an average width of 1.67 μm. Energy dispersive X-ray (EDX) analysis of AlGa-25, AlGa-50 and AlGa-75 showed 32 wt.%, 56 wt.%, and 77 wt.% of Ga_2O_3 respectively. These values confirmed the XPS results presented in Section 3.3. In the case of the AlGa-100 sample, the average size of the well-defined micro-prisms diminished significantly to an average length of 0.48 μm and an average width of 0.23 μm. Besides, the resulting material was highly homogeneous.

### 3.6.2. High-resolution transmission electron microscopy (HRTEM)
3.6.2.1. AlGa-x support series. The micrograph labeled Fig. 7A shows the typical amorphous surface of the γ-Al_2O_3 phase containing materials. This image belongs to the AlGa-0 calcined sample. The micrographs labeled 7B and 7C correspond to AlGa-25 and AlGa-50 samples, respectively. Crystal lattice observation allowed to obtain the lattice spacing (d_s) values. Three d_s preferential values were determined: 1.4 Å, 2.3 Å, and 2.5 Å. From these, the values 1.4 Å and 2.5 Å were in good agreement with planes (3 0 0) and (1 1 0) of the α-Ga_2O_3 crystallographic data sheet (JCPDS 01-074-1610), confirming the presence of this phase. Similar to the XRD results mentioned previously for samples with higher Ga_2O_3 loadings. This result allowed to propose the presence of short range crystallinity. Besides, the presence of two zones was identified, firstly the γ-Al_2O_3 and secondly mixed zones, probably related to γ-Al_2O_3-Ga_2O_3 solid solutions. In the mixed areas, a slightly lower d_s (2.3 Å) was observed, confirming the differences with the pure α-Ga_2O_3 and γ-Al_2O_3. Takahashi et al. [31] reported a d_s of around 2.4 Å for γ-Al_2O_3-Ga_2O_3 solid solutions. Thus, it is difficult to differentiate the zones belonging to the α-Ga_2O_3 phase from those coming from the solid solution, specifically in these materials.

Interestingly, the AlGa-100 +HRTEM micrographs displayed the formation of several well-defined porous micro-crystallites (Fig. 8). The average measured length was 573 ± 61 nm, and the average width was 189 ± 26 nm. Moreover, the high-resolution images showed the formation of a preferential (1 1 0) plane all over the surface. This was further confirmed by the electron diffraction pattern.

3.6.2.2. HRTEM of NiW/AlGa-x sulfided catalysts. Fig. 9 shows representative HRTEM micrographs of the pre-sulfided NiW/AlGa-x catalysts. In these images, the presence of typical structures of the layered WS_2 phase (black lines) seem to be heterogeneously distributed over different areas of the samples. The dispersion is normally related to the ratio between the number of surface metal atoms and the total number of metal atoms upon the support [32]. Therefore, it can be directly related to the length (L) and the stacking number (N) of the WS_2 nano-slabs. The mean stacking layer and length distribution of crystallites for NiW/AlGa-x samples are presented as supplementary information (S2). The statistical results are summarized in Table 3 along with the slab surface density (S_D). For NiW/AlGa-0, the slabs seemed to show a higher dispersion degree than for the other sulfided samples; the nano-slabs were homogeneously dispersed over the surface with medium stacking (2.61 ± 0.17) and the smallest length of the series (1.48 ± 0.14 nm). For NiW/AlGa-25 some slabs were formed along the planes associated with the γ-Al_2O_3–α-Ga_2O_3 solid solution or α-Ga_2O_3; however, preferential zones of distribution were absent. In the case of the NiW/AlGa-50, NiW/AlGa-75, and NiW/AlGa-100 samples, the nano-slab average length, and the stacking degree increase almost linearly respect to the gallium oxide content. Moreover, in the NiW/AlGa-75 and NiW/AlGa-100 samples a lot of long slabs forming onion-like WS_2 layers was observed. This result reflects the high tungsten coverage in these materials due to their low surface area, especially that found in the NiW/AlGa-100 sample. L values increased with the rise in gallium oxide content; noteworthy, the trend was close to linear behavior. For the stack-
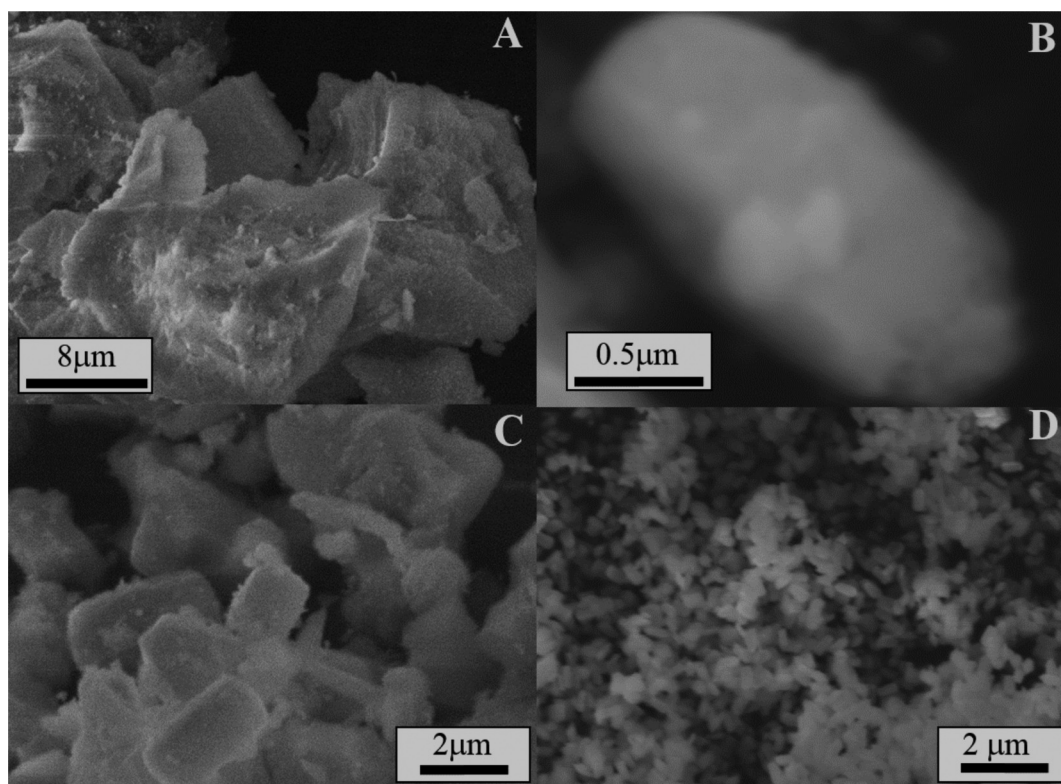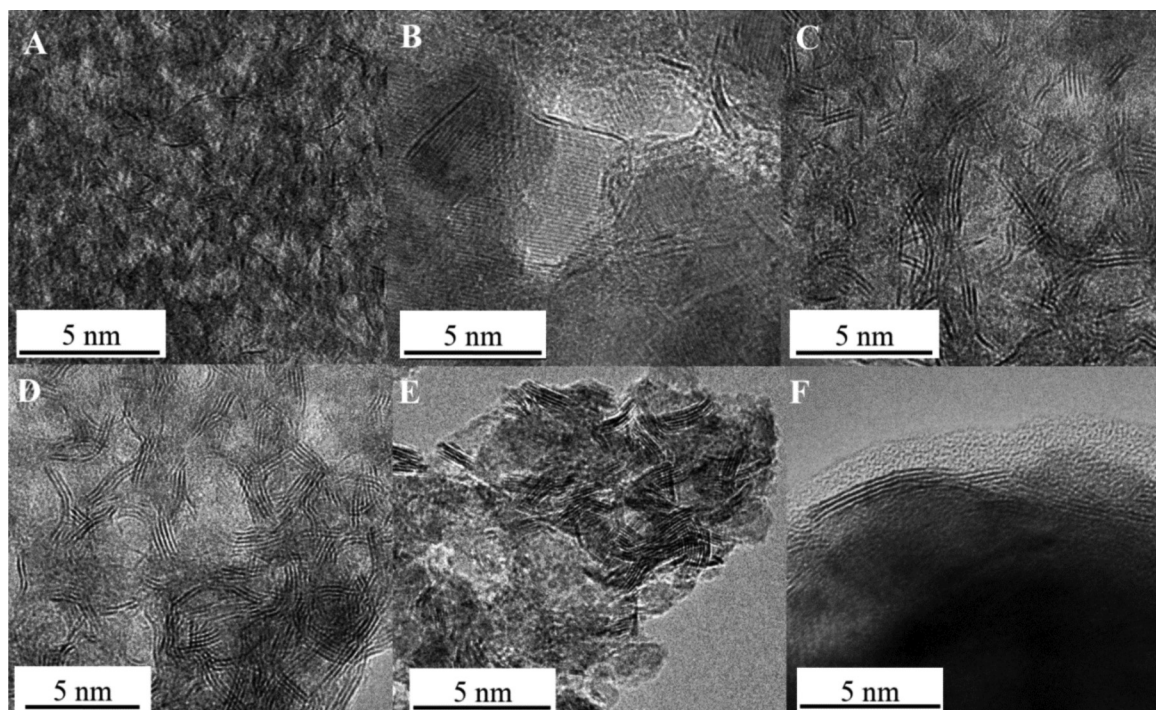
Fig. 6. SEM images of AlGa-*x* series, (A) AlGa-0, (B) AlGa-50, (C) AlGa-75, (D) AlGa-100.
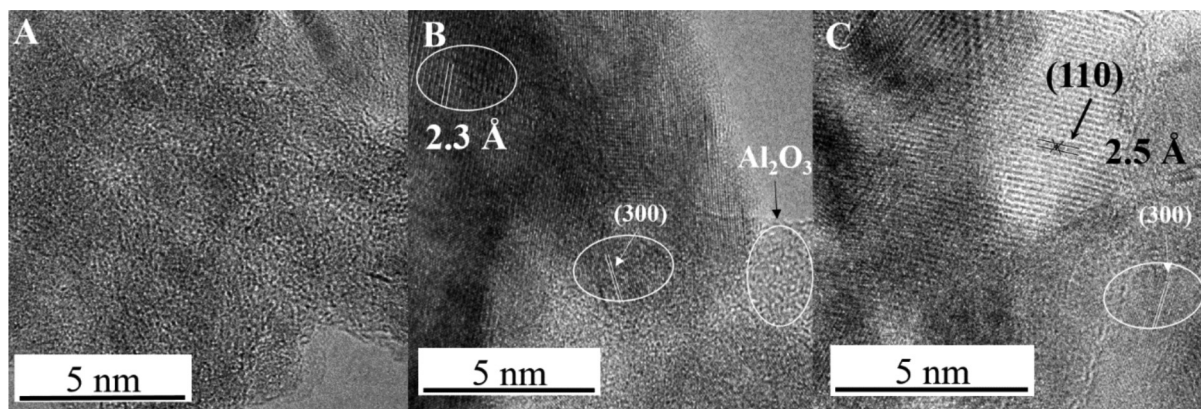
Fig. 7. Typical HRTEM micrographs for (A) AlGa-0 (B) AlGa-25 and (C) AlGa-50.
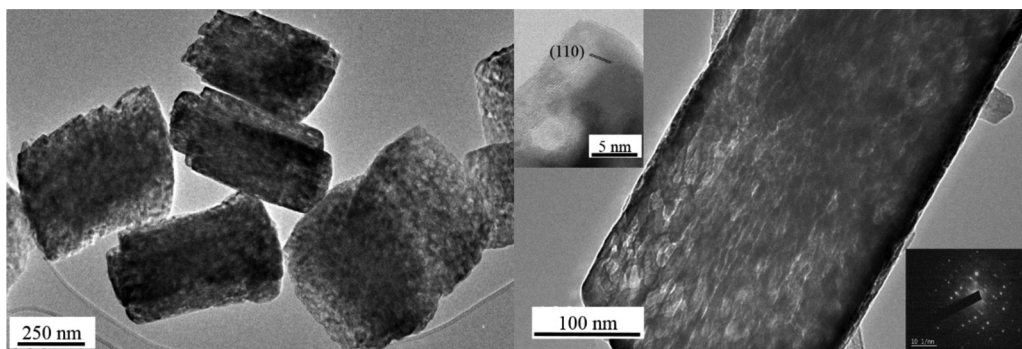
Fig. 8. Porous micro-crystallites observed by HRTEM on the AlGa-100, as inset is provided a high-resolution micrograph with the plane (1 1 0) identification and the electron diffraction pattern obtained for this zone.

Fig. 9. Representative HRTEM micrographs obtained for selected pre-sulfided NiW catalysts supported on (A) AlGa-0, (B) and (C) AlGa-25, (D) AlGa-50, (E) AlGa-75 and (F) AlGa-100.

Table 3
Average WS_2 slab length, stacking number and slab surface density for NiW/AlGa-x sulfided samples.

NiW/	AlGa-0	AlGa-25	AlGa-50	AlGa-75	AlGa-100
L[nm]	1.48 ± 0.14	1.51 ± 0.21	1.80 ± 0.18	2.32 ± 0.23	4.36 ± 0.33
N	2.61 ± 0.17	2.35 ± 0.13	2.46 ± 0.16	3.34 ± 0.19	4.35 ± 0.11
SD [WS2(particles). $500\,nm^{-2}$]	72 ± 4	67 ± 4	97 ± 6	144 ± 9	48 ± 3

ing degree, the NiW/AlGa-0 showed an N value of 2.61 ± 0.17, i.e., in the typical range reported for NiW catalysts supported on γ-Al_2O_3 [12]. The NiW catalysts supported on AlGa-25 and AlGa-50 showed the lowest N values of the series. Particularly, NiW/AlGa-25 exhibited almost 60% of its slab distribution in the range of 2–3 stacks. The values obtained for the slab surface density in Table 3 are worth mentioning. The S_D value quantitatively shows the exact distribution of the active phase over the surface as the number of WS_2 particles per unit of area. As seen, the NiW/AlGa-0 sample presented an S_D value of 72 ± 4 particles per $500\,nm^2$, the S_D value slightly decreased to 67 ± 4 for NiW/AlGa-25. When Ga_2O_3 increased, S_D increased as well until values as high as 144 ± 9 particles per $500\,nm^2$ were obtained. The NiW/AlGa-100 sample showed a low S_D value of 48 ± 3 particles per $500\,nm^2$. This low value coincided with the morphology observed in Fig. 9F where highly stacked and long WS_2 slabs were observed.

4. Catalytic activity tests

4.1. Diesel model compound hydrodesulfurization

The catalytic activity results are listed in Table 4. The influence of gallium oxide loading was directly reflected on the catalytic activity: 18% higher for the NiW/AlGa-25 sulfided catalyst compared with the Ga_2O_3-free sample (NiW/AlGa-0). Further gallium oxide loading rendered a decrease in catalytic activity. However, selectivity displayed a clear modification. Sulfur removal from hydrocarbons usually occurs by two pathways, hydrogenation (HYD), and direct desulfurization (DDS). For the DBT, desulfuriza-

tion normally tends to be by DDS, as observed for NiW/AlGa-0, despite the hydrogenation properties of the NiW system [7,13]. Considering the rates, r_{HID}, r_{DSD}, and selectivity ratios, $S_{HYD/DSD}$, the effect of Ga_2O_3 loading was directly reflected on the HYD pathway. While the increase in r_{HID} was approximately 46%, for the r_{DSD} it was only 26% for the material with highest catalytic activity (NiW/AlGa-25). The effect of gallium loading was more evident when comparing the $S_{HYD/DSD}$, while for NiW/AlGa-25 the value was 0.21, for the NiW/AlGa-75 catalyst it was 0.37. Also, the $S_{HYD/DSD}$ for NiW/AlGa-25 was lower than the reported $S_{HYD/DSD}$ value for the NiW/Al_2O_3 commercial catalyst [7] indicating a lower H_2 consumption.

4.2. Gasoline model compound hydrodesulfurization

The influence of the support on the NiW catalysts was tested in the hydrodesulfurization reaction of 3MT as a gasoline model compound. The steady state catalytic rates plotted versus the Ga content displayed a volcano curve where the NiW/AlGa-25 sample showed the highest value (292.6×10^{-8} $mol_{3MT}\, g_{cat}^{-1}\, s^{-1}$) of the series (see Supplementary information Fig. S3). This material revealed 22% more activity than NiW/AlGa-0 and 13% more than NiW/AlGa-50. An additional increase of gallium oxide content decreased the catalytic activity for the remaining sulfided samples. The selectivity values were clearly modified by the presence of the Ga_2O_3 as in the case of the DBT reaction. The 3MT HDS reaction occurs via parallel pathways involving direct hydrogenation (HYD) and direct desulfurization (DDS) with two subsequent hydrogenation steps, as suggested previously for CoMo catalysts [33]. The detected prod-

Table 4
DBT initial reaction rate, yield and selectivity dependence with the Ga_2O_3 content.

NiWS Catalyst	$r_{DBT}[mol_{DBT} \, g_{cat}^{-1} \, s^{-1}]$	r_{HYD}	r_{DDS}	$S_{HYD/DDS}$
AlGa-0	72.2	10.9	61.3	0.18
AlGa-25	85.2	14.5	70.7	0.21
AlGa-50	70.8	14.3	56.5	0.25
AlGa-75	34.3	9.2	25.0	0.37
AlGa-100	14.3	4.5	9.8	0.46
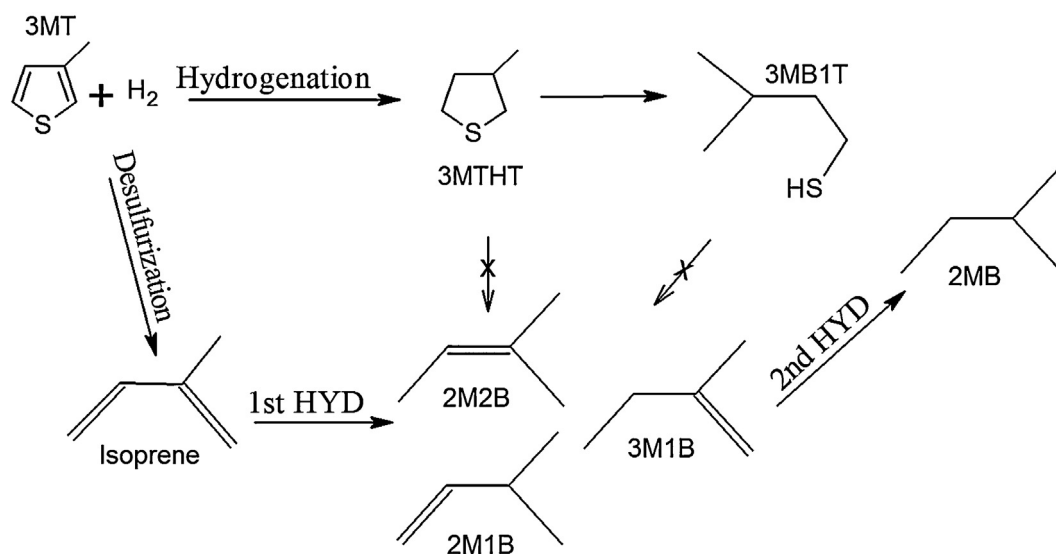
Scheme 1. Reaction path network for the 3-methyl-thiophene over the pre-sulfided NiW/AlGa-x materials.

Table 5
3MT Steady state reaction rates, selectivity and DDS product yield.

| NiW Catalysts	Steady state reaction rate at 280 °C	Selectivity at 280 °C		DDS Product yield%		
	$x10^{-8} \, mol_{3MT} \, g_{cat}^{-1} \, s^{-1}$	HYD	DDS	Isoprene	C_5-Olefins	iC_5-parafin
AlGa-0	239.9	1.0	99.0	24.07	75.33	0.61
AlGa-25	293.2	3.8	96.2	17.76	78.52	3.72
AlGa-50	258.5	6.4	93.6	16.67	78.69	4.65
AlGa-75	219.6	8.9	91.1	15.10	78.81	6.09
AlGa-100	136.7	17.5	82.5	16.48	79.05	4.46

ucts were divided in two reaction routes: for HYD, the 3-methyl tetrahydrothiophene (3MTHT) and the 3-methyl-butane-1-thiol (3MB1T) pathways. The DDS route produced only isoprene; nevertheless, this desulfurized product derived into iso-olefins (C5-i) such as 2-methyl 2-butene (2M2B), 2-methyl 1-butene (2M1B) and 3-methyl 1-butene (3M1B). Moreover, 2-methyl butane (2MB), an iso-aliphatic hydrocarbon compound was also produced. Scheme 1 shows the reaction path network based on the detected products. Catalytic activity, selectivity, and yield are summarized in Table 5.

As expected, the highest catalytic activity for the series was displayed by the NiW/AlGa-25 sulfided sample, almost 22% higher than NiW/AlGa-0. Further increase in gallium content diminished the steady state reaction rate for NiW/AlGa-100 (2.14 times) in comparison with NiW/AlGa-25. It should be noted that the main reaction pathway for all materials was the DDS. However, the initial HYD path (3MTHT and 3MB1T) increased almost linearly with gallium oxide content, from 1% for NiW/AlGa-0 to 17.5% for NiW/AlGa-100. Once the initial DDS was completed, isoprene production diminished by successive hydrogenation steps. Therefore, it is important to note that all samples produced between 75 and 79% of C5-olefin. Only for NiW/AlGa-75 did the production of iC5-parafin reach 6%. The average production of isoprene was approximately constant (18%), except for NiW/AlGa-0 with 25%.

Finally, the production of C5-olefins slightly increased with the gallium oxide content.

5. Discussion

After thermal treatment at 773 K, the AlGa-x series of materials exhibited suitable textural properties for preparing the HDS catalysts (Table 1). The pore width distribution for AlGa-25 and AlGa-50 (Fig. 1b) showed a very sharp unimodal distribution. In particular, AlGa-25 displayed the highest surface area of the series and among materials prepared with similar methodology elsewhere [19,23]. Previous reports show that different Ga_2O_3 phases are obtained from a wide variety of precipitating agents. Thus, Masuda et al. [23] reported the preparation of γ-Ga_2O_3–Al_2O_3 solid solutions and a mixture of β and γ phases of Ga_2O_3 calcining at 973 K. Results reported here revealed that using NH_4OH as a precipitant agent, the pure α-Ga_2O_3 phase was successfully obtained after calcinations at only 773 K. Furthermore, as shown by XRD results, a γ-Ga_2O_3–Al_2O_3 solid solution was obtained by this modified method for materials AlGa-25 and AlGa-50. Nevertheless, as indicated by XPS results, the measured Ga/(Ga + Al) atomic ratio was higher than the theoretical values for these samples, meaning that gallium-rich zones were present on the surface. On the other hand,
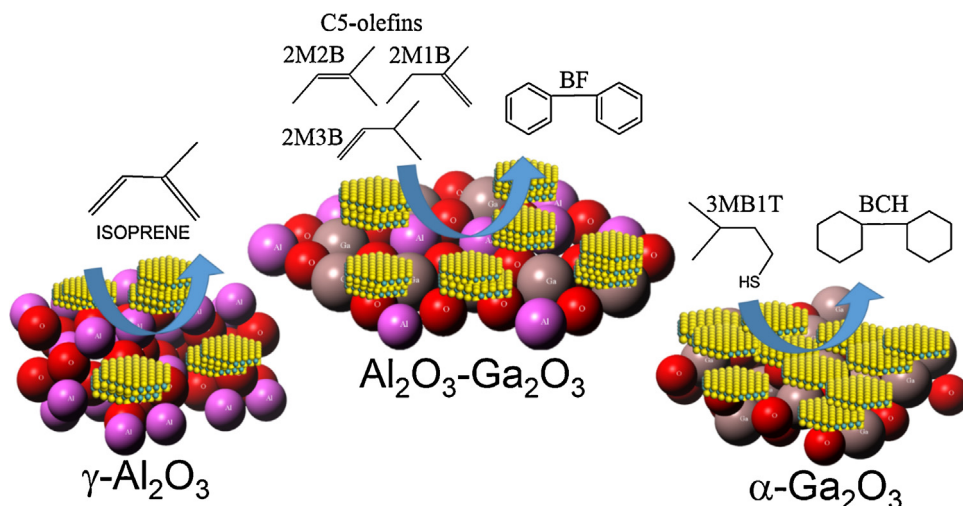
Scheme 2. Schematic representation of the catalytic systems and main yield. The atoms are not to scale, and the sizes only are illustrative.

the SEM-EDS results indicated that samples AlGa-25 and AlGa-50 were slightly gallium-enriched, which confirmed the XPS analysis. These findings indicate the presence of a mixed Al_2O_3–Ga_2O_3 solid solution. Also, the modification of the PZC of calcined samples suggested the existence of superficial $GaAl_2O_4$ spinels due to the low observed IEP. The presence of this spinel type compound is related to the occupation of Ga^{3+} ions of tetrahedral sites in the alumina packing. Earlier studies reported that gallium has a preference for tetrahedral sites in the Al_2O_3 structure [34]. The preference of Ga^{3+} (radius 0.61 Å) for fourfold coordination, despite the fact that it has larger radius than Al^{3+} (0.53 Å), could be related with the polarizing influence of the d^{10} core; a similar tetrahedral site preference is also observed for Fe^{3+} [35]. Therefore, a solid solution would be easy to form by crystal lattice substitution, where aluminum is replaced by gallium or inversely. Besides, the formation of spinel-type solid solutions seems to play a fundamental role in the dispersion and distribution of surface gallium sites on Al_2O_3–Ga_2O_3 materials [36]. HRTEM morphological studies were consistent with the results discussed above. The micrographs revealed zones of γ-Al_2O_3, α-Ga_2O_3 and zones assigned to the mixed phase. For the AlGa-75 sample, the α-Ga_2O_3 began to be slightly segregated from the γ-Al_2O_3 phase. The SEM images showed the formation of microcrystals with prismatic shape in the higher gallium oxide content materials. Remarkably, as the Ga_2O_3 content of the samples increased, the clearer formation of micro-crystals was visible. The images presented in Fig. 9 confirm the initial SEM observations. The production of well-defined particles is in good agreement with recent studies of α-GaOOH units and their calcination products [37].

HRTEM images of the sulfide catalysts showed the good dispersion of the WS_2 sulfide phase, especially in the NiW/AlGa-25 sample. This may be explained considering that this material displayed the lowest ZPC. The presence of the mentioned $GaAl_2O_4$ spinels can improve the dispersion of the octahedral polytungstate species. Recent studies indicate that the electrostatic interaction of the surface with the W-hydroxide species (as the anionic $HW_6O_{21}^{5-}$) becomes stronger with materials that possess a lower ZPC than the γ-Al_2O_3 [11]. Based on previous results, a schematic view of the samples (Scheme 2) was proposed. The γ-Al_2O_3 structure (AlGa-0) was simulated considering a 3D hexagonal lattice. For α-Ga_2O_3 (AlGa-100), its structure was simulated from a 3D monoclinic lattice. In addition, the scheme shows the image of a possible Al_2O_3–Ga_2O_3 solid solution. The scheme includes typical WS_2 slabs considering the L and N values obtained by statistical analysis of the HRTEM.

DBT catalytic activity for NiW/AlGa-0 was found to be similar to that reported for the NiW catalyst prepared using commercial alumina [12]. However, to compare the catalytic activity fairly, it should be noted that the catalysts were prepared with slightly less W content than the reference, i.e., 16 wt.% for our samples and 20 wt.% for the industrial reference catalyst [7]. From the NiW/AlGa-series, the use of AlGa-25 support provided the highest specific activity among the tested samples with 18% and 22% more than the gallium-free catalyst in hydrodesulfurization of DBT and 3MT, respectively. The catalytic activity results shown by the NiW/AlGa-x sulfided catalyst in the HDS of 3MT at atmospheric pressure are relevant because the production of gasoline is normally derived from the fluid catalytic cracking (FCC) naphtha. Which in addition to undesired organic sulfur compounds are rich in olefins that help to meet the high octane number requirements. Consequently, sulfur removal avoiding olefin saturation is necessary; besides, conventional fixed bed hydrodesulfurization units can reduce the sulfur level of cracked naphtha to very low concentrations operating at high hydrogen pressure. However, a typical result is an unwanted octane loss because of excessive hydrogenation of olefins [38]. Under atmospheric pressure, the H_2 coverage of the surface would be very low and undesirable olefin saturation would be avoided. The NiW/AlGa-x catalysts displayed high hydrodesulfurization activity under these mild conditions, and the main reaction pathway resulted in direct desulfurization.

5.1. Support-selectivity correlation

As shown, the morphological analysis suggests a good dispersion of the WS_2 active phase in the NiW/AlGa-25 sulfided material, consistent with the activity results. The inclusion of Ga_2O_3 in the alumina support probably helped to weaken the interaction between the active phase and the support, particularly in the NiW/AlGa-25 catalyst. The selectivity showed an enhancement of the HYD pathway with the increase of Ga_2O_3 wt.% in both reactions; nevertheless, activity decreased considerably for NiW/AlGa 100. This was probably due to the agglomeration of the WS_2 slabs, related to the aforementioned decrease in the interaction between the active phase and the support as well as the observed decrease in textural properties. The NiW/AlGa-100 catalyst exhibited high surface coverage, since 16 wt.% W loading would mean c.a. 16 W atoms per square nanometer. The effect of the gallium on the surface was more evident in the 3MT HDS reaction, as the HYD route increased almost linearly with the Ga_2O_3 content, as well as the HYD steps that follow after initial direct desulfurization. Nevertheless, only
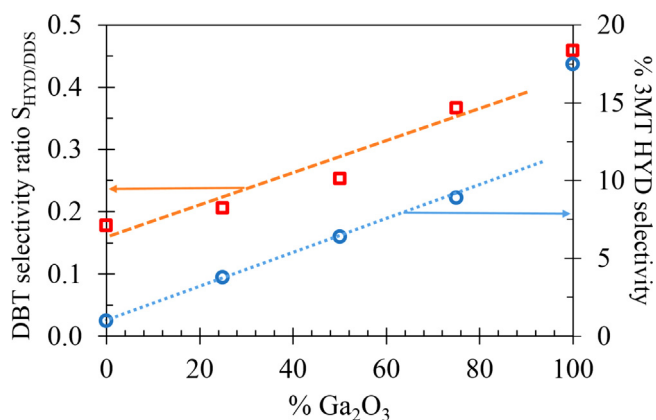
Fig. 10. Dependence of the selectivity upon Ga_2O_3 content in NiW catalysts. Dotted lines indicate the observed tendency.

traces of the aliphatic paraffin (2MB) were observed, suggesting a mild HYD capacity. The large production of C_5-olefins could be related to the desulfurization of the 3MTHT; nonetheless, the formation of thiols was (as in the case of the 2MB) very low, and only traces were detected. It was recently reported that the chemical and electronic properties of the support could impact the sulfide phase size [39]. Also, it is widely recognized that the stacking height plays a key role in catalytic activity [40]. Therefore, the aforementioned variation of catalytic hydrogenation for both reactions might be related to the length and stacking [40]. Indeed, the DBT selectivity ratio $S_{HYD/DDS}$ and the% 3MT HYD selectivity correlate well with the changes observed in the WS_2 slabs morphology (See Supplementary information S4). Nevertheless, as mentioned above, these changes in WS_2 morphology derive from the support modification. Therefore, Fig. 10 presents how the selectivity toward hydrogenation increases linearly in both reactions with the increase in Ga_2O_3 content in the NiW catalysts.

6. Conclusions

The textural properties of the mixed supports are suitable for the preparation of hydrodesulfurization catalysts. The AlGa-*x* materials with $x \geq 25\%$ presented single microcrystallites and a great quantity of arrays of rectangular prism-shaped particles. Especially, the α-Ga_2O_3 (AlGa-100) presented the smallest microcrystallites of the series. The XRD results confirmed the formation of the Al_2O_3–Ga_2O_3 solid solution, at least in materials AlGa-25 and AlGa-50. Further increase of Ga_2O_3 content led to a phase segregation. Based on the XPS and the ZPC results, the formation of $GaAl_2O_4$ spinels all over the surface is proposed. The gallium oxide surface enrichment impacts on the dispersion and length of the WS_2 nano-slabs. The results presented here, particularly the catalytic activity, have shown that AlGa-25 has high potential as support for NiW sulfur removal catalysts. Further characterizations are in progress to fully explain the observed results, mainly those concerning the acidity/basicity contribution of Ga_2O_3 to the supports and the catalytic system.

Acknowledgements

Appendix A. Supplementary data

Supplementary data associated with this article can be found, in the online version, at http://dx.doi.org/10.1016/j.apcatb.2015.08.028.

References

[1] D. Laurenti, B. Phung-Ngoc, C. Roukoss, E. Devers, K. Marchand, L. Massin, L. Lemaitre, C. Legens, A. Quoineaud, M. Vrinat, J. Catal. 297 (2013) 165–175.
[2] J. Ancheyta-Juarez, E. Aguilar-Rodriguez, D. Salazar-Sotelo, G. Betancourt-Rivera, M. Leiva-Nuncio, Appl. Catal. A: Gen. 180 (1999) 195–205.
[3] G.C. Laredo, P.M. Vega-Merino, F. Trejo-Zárraga, J. Castillo, Fuel Process. Technol. 106 (2013) 21–32.
[4] Y. Gwang-Nam, L. Yong-Kul, Appl. Catal. B: Environ. 150–151 (2014) 647–655.
[5] Z. Vít, L. Kaluza, D. Gulkova, Fuel 120 (2014) 86–90.
[6] T.A. Zepeda, B. Pawelec, J.N. Díaz de León, J.A. de los Reyes, A. Olivas, Appl. Catal. B: Environ. 111–112 (2012) 10–19.
[7] J.N. Díaz de León, V. Petranovskii, J.A. de los Reyes, G. Alonso-Nuñez, T.A. Zepeda, S. Fuentes, Appl. Catal. A: Gen. 472 (2014) 1–10.
[8] O.Y. Gutiérrez, S. Singh, E. Schachtl, J. Kim, E. Kondratieva, J. Hein, J.A. Lercher, ACS Catal. 4 (2014) 1487–1499.
[9] H. Topsoe, B.S. Clausen, F.E. Massoth, Hydrotreating Catalysis, Springer, Berlin, 1996.
[10] E. Altamirano, J.A. de los Reyes, F. Murrieta, M. Vrinat, Catal. Today 133–135 (2008) 292–298.
[11] J.N. Díaz de León, M. Picquart, M. Villarroel, M. Vrinat, F.J. Gil Llambias, J.A. de los Reyes, J. Mol. Catal. A-Chem. 323 (2010) 1–6.
[12] J.N. Díaz de León, M. Picquart, L. Massin, M. Vrinat, J.A. de los Reyes, J. Mol. Catal. A Chem. 363–364 (2012) 311–321.
[13] L. Kaluža, R. Palcheva, A. Spojakina, K. Jirátová, G. Tyuliev, Procedia Eng. 42 (2012) 873–884.
[14] M. Breysse, C. Geantet, P. Afanasiev, J. Blanchard, M. Vrinat, Catal. Today 130 (2008) 3–13.
[15] T. Olorunyolemi, R.A. Kydd, J. Catal. 158 (1996) 583–586.
[16] T. Olorunyolemi, R.A. Kydd, Catal. Lett. 63 (1999) 173–178.
[17] Y.C. Park, H.K. Rhee, Appl. Catal. A: Gen. 179 (1999) 145–153.
[18] T. Nakatani, H. Deguchi, T. Watanabe, S. Iwamoto, M. Takahashi, H. Kanai, Y. Miyahara, M. Inoue, J. Phys. Chem. A 113 (2009) 7021–7029.
[19] I. Geukens, F. Vermoortele, M. Meledina, S. Turner, G.V. Tendeloo, D.E. De Vos, Appl. Catal. A: Gen. 469 (2014) 373–379.
[20] D.G. Barton, M. Stein, R.D. Wilson, S.L. Soled, E. Iglesia, J. Phys. Chem. B 103 (1999) 630–640.
[21] J.M. Miller, L.J. Lakshmi, J. Phys. Chem. B 102 (1998) 6465–6470.
[22] IUPAC recommendations, Pure Appl. Chem. 57–4 (1985) 603–619.
[23] T. Masuda, T. Watanabe, Y. Miyahara, H. Kanai, M. Inoue, Top. Catal. 52 (2009) 699–706.
[24] C. Otero Arean, A. Lopez-Bellan, M. Peñarroya-Mentruit, M. Rodriguez-Delgado, G. Turnes-Palomino, Microporous Mesoporous Mat. 40 (2000) 35–42.
[25] M. Kosmulski, Adv. Colloid Interface Sci. 152 (2009) 14–25.
[26] B. Inceesungvorn, J. López-Castro, J.J. Calvino, S. Bernal, F.C. Meunier, C. Hardacre, J.J. Delgado, K. Griffin, Appl. Catal. A: Gen. 391 (2011) 187–193.
[27] C. Otero Arean, M. Rodríguez Delgado, V. Montouillout, D. Massiot, Z. Anorg. Allg. Chem. 631 (2005) 2121–2126.
[28] Y. Hou, L. Wu, X. Wang, Z. Ding, Z. Li, X. Fu, J. Catal. 250 (2007) 12–18.
[29] S. Kumar, C. Tessarek, S. Christiansen, R. Singh, J. Alloy Compd. 587 (2014) 812–818.
[30] D.M. Christie, J.R. Chelikowsky, Phys. Rev. B 62 (2000) 14703.
[31] M. Takahashi, N. Inoue, T. Takeguchi, S. Iwamoto, M. Inoue, J. Am. Ceram. Soc. 89 (2006) 2158–2166.
[32] James J. Carberry, Chemical and Catalytic Reaction Engineering, McGraw-Hill, New York, 1976, pp. 423.
[33] N. Dos Santos, H. Dulot, N. Marchal, M. Vrinat, Appl. Catal. A Gen. 352 (2009) 114–123.
[34] A. Cimino, M. Lo Jacono, M. Schiavello, J. Phys. Chem. 79 (3) (1975) 243–249.
[35] G.H. Robinson, Gallium: organometallic chemistry, in: Encyclopedia of Inorganic Chemistry, 2nd ed., Wiley Ed., 2005, pp. 1363.
[36] M. Chen, J. Xu, F.Z. Su, Y.M. Liu, Y. Cao, H.Y. He, K.N. Fan, J. Catal. 256 (2008) 293–300.
[37] aM. Rsitic, S. Kubuki, Y. Lida, M. Fabian, S. Music, J. Alloy Compd. 620 (2015) 217–227.
[38] G. Brignac T.R. Halbert J.P. Greeley US patent, 20090166263A1.
[39] J.N. Díaz de León, T.A. Zepeda, G. Alonso-Nuñez, D.H. Galván, B. Pawelec, S. Fuentes, J. Catal. 321 (2015) 51–61.
[40] M. Daage, R.R. Chianelli, A.F. Ruppert, Stud. Surf. Sci. Catal. 75 (1993) 571–584.